Journal of Electronic Materials (2022) 51:6320–6332
https://doi.org/10.1007/s11664-022-09851-w

ORIGINAL RESEARCH ARTICLE

High Thermoelectric Properties of Janus WSeS Bilayer Membranes with Different Stacking Modes

Mingchang Li[1] · Xihao Chen[2] · Liang Zhang[1]

Received: 25 April 2022 / Accepted: 25 July 2022 / Published online: 2 September 2022
© The Minerals, Metals & Materials Society 2022

Abstract

The two-dimensional WSeS membrane is considered a promising Janus material with many potential applications in the area of thermoelectric energy due to the unique electrical and thermal transport capability originating from structural asymmetry. Thus, the thermoelectric properties of Janus-based WSeS bilayers, including three types of combination modes, namely, SWSe/SWSe (SeS stacking), SWSe/SeWS (SeSe stacking), and SeWS/SWSe (SS stacking), were thoroughly investigated by performing first-principles calculations based on the semiclassical Boltzmann transport theory in conjunction with the relaxation time approximation method. The Janus WSeS bilayer structures exhibit excellent electrical transport capability and thermoelectric properties because the deformation potential constant and elastic modulus of the monolayers result in a long carrier relaxation time. The figure of merit (ZT) of the SeSe-based structure is as high as 2.4 at 900 K with an n-type doping concentration of $5 \times 10^{11} cm^{-3}$ due to lower lattice thermal conductivity and higher electrical conductivity compared with the other two stacking configurations. This study provides a strategy for evaluating the thermal energy conversion efficiency for various thermoelectric applications.

Keywords Janus WSeS bilayer · stacking modes · electronic transport properties · thermal transport properties · thermoelectric properties

Introduction

The consumption of thermal energy from traditional fossil fuels is currently the most important means of electricity generation worldwide. However, the disadvantages of this form of electricity generation, which include low efficiency and environmental pollution, are becoming increasingly prominent. As a result, there is an urgent need to replace this conventional method of energy generation with novel clean energy generation schemes. Thermoelectric materials provide a type of green electricity that meets this requirement.[1–3] The thermoelectric conversion capacity of these materials can be measured in terms of the optimal value of thermoelectricity, which can be expressed as $ZT = S^2 T\sigma/\kappa$.[4,5] In this formula, S is the Seebeck coefficient, σ is the electrical conductivity, T is the absolute temperature, and κ is the thermal conductivity. Note that both the electronic thermal conductivity κ_e and the lattice thermal conductivity κ_l contribute to the total thermal conductivity distribution.[6]

A large number of theoretical and experimental studies have been conducted over more than a decade on the thermoelectric properties of nanomaterials. Two-dimensional (2D) layered nanomaterials possess good electronic, mechanical, and chemical properties, such as a large surface area and abundant active centers,[7] and are therefore extremely interesting to the scientific community.[8–10] For example, a 2004 study showed that peeled-off single-layer graphene exhibited excellent physical properties, such as high fluidity and enhanced mechanical and chemical stability. However, the standard thermoelectric applications of graphene are limited by a small electron gap. Consequently, intensive research is being conducted to enlarge the graphene band gap.[11,12] At the same time, there is considerable demand for the development of novel types of two-dimensional (2D) graphene-like materials for fabricating novel thermoelectric materials. One such graphene-like material that has been attracting increasing interest from the scientific community consists of low-dimensional layered transition metal halide (TMD) structures, especially Janus TMD structures.[13–15]

✉ Liang Zhang
zhangliang545@sqnu.edu.cn

1 School of Electronic & Electrical Engineering, Shangqiu Normal University, Shangqiu 476000, China

2 School of Materials Science and Engineering, Research Institute for New Materials and Technology, Chongqing University of Arts and Sciences, Chongqing, China

There are different chalcogenide elements of the Janus TMD on the two sides of the transition metal, which breaks the mirror symmetry of the structure. Interestingly, this asymmetry increases the carrier mobility and lowers the thermal transport capacity, enhancing the thermoelectric properties. Patel et al. carried out first-principles calculations based on the semiclassical Boltzmann transport theory to investigate WSSe and WSTe Janus monolayers.[16] The WSTe Janus monolayers exhibited the highest *ZT* of 2.56 at a high temperature. This effect was ascribed to the combination of the high electrical conductivity, high Seebeck coefficient and very low lattice thermal conductivity of the Janus WSTe monolayers.[16] Chaurasiya et al. investigated the impact of strain on the thermoelectric properties of Janus WSeS monolayers by using a self-consistent method in conjunction with the single-mode relaxation time approximation (RTA).[17] The extracted outcomes showed that the *ZT* of n(p) carriers increased from 0.72 (0.73) to 1.06 (1.08) at concentrations of $5 \times 10^{20}\text{cm}^{-3}$ ($7 \times 10^{20}\text{cm}^{-3}$) under an applied biaxial strain. This effect is attributed to the characteristics of the valence band and the valence band edges obtained under a biaxial strain, few valleys in the energy band structure, and an enhanced power factor.[17] Holt et al. employed the advanced planar linearization (FP-LAPW) method and Boltzmann's semiclassical transmission theory to study the HfSSe-Janus structure, where a first principles calculation was used to determine the electronic structure and optical and thermoelectric properties of a single layer.[18] Under the application of a −4% compressive strain, the power factor (PF) value of the n-doped materials was 4.570 $\text{Wm}^{-1}\,\text{K}^{-2}\,\text{s}$ ($PF = S^2\sigma$) at 800 K, because metals with free electrons exhibit relatively high electrical conductivity under stress.

All the abovementioned studies were performed on materials with excellent thermoelectric properties, whereas there have been no reports of the thermoelectric properties of Janus-based WSeS bilayer structures with different stacking modes. Thus, three combination modes of WSeS bilayer configurations, namely, SWSe/SWSe (SeS stacking), SWSe/SeWS (SeSe stacking), and SeWS/SWSe (SS stacking), are investigated in this study by conducting first-principles calculations based on the relaxation time approximation method. The thermal conductivity, electrical conductivity, and Seebeck coefficient of the three structures are systematically investigated at different temperatures and doping concentrations. The calculation results demonstrate that the WSeS bilayers with SeSe stacking possesses the highest *ZT* and can be employed as a candidate material for future thermoelectric applications.

Computational Methods

Calculations were performed in this study using the Vienna Ab Initio Simulation Package (VASP) with the generalized gradient approximation and the Perdew–Burke–Ernzerhof (PBE) exchange–correlation (XC) functional.[19,20] The Heyd–Scuseria–Ernzerhof (HSE06) static self-consistent hybridization generalization method was used to accurately calculate the energy band structure.[21] The Seebeck coefficients and electrical transport properties of the investigated materials were calculated by the BoltzTrap2 program using the semiclassical Boltzmann transport equation (BTE) and RTA method.[22,23] The relaxation times of the carriers were estimated using deformation potential (DP) theory.[24] The semiempirical corrections in the GRIMME DFT-D3 model were utilized to describe the weak van der Waals (vdW) interactions between two layers of the Janus WSeS nanostructure.[25] In the optimized simulation, a cutoff energy of 500 eV and a $15 \times 15 \times 1$ k-point grid were used to model the Brillouin zone. The electron transport properties were estimated using a $30 \times 30 \times 1$ Monkhorst–Pack special k-point grid. The phonon dispersion and transport properties were calculated using a $3 \times 3 \times 1$ supercell and a $3 \times 3 \times 1$ Monkhorst–Pack special k-point grid by the Phonopy and Phono3py software packages.[26,27] The moment of the *a*-th generalized transmission coefficient $\pounds^{(a)}$ was calculated as

$$\pounds^{(a)}(u;T) = q^2 \int \sigma(\varepsilon, T)(\varepsilon - u)^{\alpha} \left(-\frac{\partial f^{(0)}(\varepsilon;u,T)}{\partial \varepsilon} \right) d\varepsilon \quad (1)$$

where ε, q, u and T are the band energy, charge, chemical potential, and temperature, respectively. The transport distribution function $\sigma(\varepsilon, T)$ is given by

$$\sigma(\varepsilon, T) = \int \sum_{b} \mathbf{v}_{b,\mathbf{k}} \otimes \mathbf{v}_{b,\mathbf{k}} \tau_{b,\mathbf{k}} \delta(\varepsilon - \varepsilon_{b,\mathbf{k}}) \frac{d\mathbf{k}}{8\pi^3} \quad (2)$$

where the summation over *b* bands is integrated over the **k** points. $\mathbf{v}_{b,\mathbf{k}}$ and $\tau_{b,\mathbf{k}}$ represent the carrier velocity and relaxation of the *b* th band at the **k** th point, respectively.

The deformation potential (DP)[24] is typically used to estimate the carrier relaxation time τ, which can be expressed as follows:

$$\tau = \frac{\mu m^*}{e} = \frac{2\hbar^3 C}{3k_B T m^* E_l^2} \quad (3)$$

where μ,$\hbar$,$m*$, C, E_l and k_B are the carrier mobility, reduced Planck constant, effective mass, elastic constant, deformation potential constant, and Boltzmann constant, respectively. The effective mass of the carrier is defined as $m^* = \hbar^2 / \left(\partial^2 E / \partial^2 k\right)$, and the elastic constant is given by

$C = \left[\partial^2 E/(\partial\varepsilon)^2\right]/S_0$, where E is the total energy of the system, $\varepsilon = \Delta l/l_0$ is the lattice strain under stress along the long x- or y-direction, and l_0 is the equilibrium lattice constant. E_l is calculated as $E_l = \partial E_{edge}/\partial\varepsilon$, where E_{edge} is the shift of the band edge.

The rigid band approximation can be used to determine an electrical transport coefficient at a specified temperature T and chemical potential ε. The carrier concentration can be calculated by the following equation:

$$n(\varepsilon) = \int \sum_b \delta(\varepsilon - \varepsilon_{b,\mathbf{k}}) \frac{d\mathbf{k}}{8\pi^3} \tag{4}$$

where the sum is performed over b bands; the deviation from charge neutrality is then calculated as

$$C(\mu, T) = N - \int n(\varepsilon) f^{(0)}(\varepsilon; \mu, T) d\varepsilon \tag{5}$$

where N is the nuclear charge and $f^{(0)}$ is the Fermi distribution function.

The electrical conductivity σ, electronic thermal conductivity κ_e, and Seebeck coefficient S can be written as follows:

$$\kappa_e = \frac{1}{q^2 T}\left[\frac{\left(\pounds^{(1)}\right)^2}{\pounds^{(0)}} - \pounds^{(2)}\right] \tag{6}$$

$$\sigma = \pounds^{(0)} \tag{7}$$

$$S = \frac{1}{qT}\frac{\pounds^{(1)}}{\pounds^{(0)}} \tag{8}$$

Results and Discussion

Geometric Structure and Phonon Spectrum

An in-depth analysis of three different combination modes of WSeS-based bilayer structures is performed in this study, namely, SWSe/SWSe (SeS stacking), SWSe/SeWS (SeSe stacking), and SeWS/SWSe (SS stacking), which are schematized as ball-and-stick models in Fig. 1a–c. These three structures exhibit 2D hexagonal lattice symmetry. Thus, each minimum cell contains six atoms. An analysis of the results of VASP calculations with GGA-PBE shows that the lattice parameters for the SeS, SeS, and SS structures are almost the same in the a- and b-directions, with approximate values of 3.22 Å. The thicknesses of the SeS, SeSe, and SS structures are 9.51 Å, 9.59 Å, and 9.45 Å, respectively. The layer spacings of the SeS, SeSe, and SS structures are 2.99 Å, 3.05 Å, and 2.92 Å, respectively. Figure 1 shows the dynamical photon properties determined after performing the optimization process. Figure 1e and f show the phonon spectra of the three structures of the Janus WSeS bilayer membrane. An analysis of the extracted outcomes shows that the entire frequency band is above 0, indicating that these three structures are stable. Ab initio molecular dynamics (AIMD) simulations demonstrated the thermodynamic stabilities of the three structures, as presented in supplementary Figs. S1–S4 in the Supplementary Materials.

Energy Band Structure and Electronic Density of States

The energy band structure and electron projected density of states (PDOS) were determined for the three types of WSeS bilayers. Figure 2 shows the energy band structure and PDOS of the WSeS bilayer determined by carrying out static self-consistent calculations based on the HSE06 hybridization generalization function with the VASP package.[28] The calculated energy band structure lies along the ΓKMΓ high-symmetry direction due to the formation of a planar hexagonal structure.[29] Figure 2a, b, and c show that the three Janus WSeS structures have an indirect band gap. The band gaps of the SeS, SeSe, and SS structures are 1.58 eV, 1.93 eV, and 1.66 eV, respectively. The peaks of the valence bands of the three structures are parabolic and flatter than those of the conduction bands, indicating the existence of relatively large hole effective masses,[30] as shown in Table I.

The band gap of the SeS structure is smaller than that of the SeSe and SS structures. This result is obtained because the different polar charge distributions of the layers create a difference between the electronegativity of the atoms at the two ends of W, resulting in electrostatic attraction between the two layers and thereby reducing the energy band gap.[32] To further analyze the electronic structure of the 2D WSeS bilayer, the PDOS of the three structures was determined and is shown in Fig. 2d, e, and f. The d orbital of the W atom plays a very important role in the conduction band of the investigated structures. This d orbital also makes a large contribution to the major valence band near the Fermi level. The p orbitals of the W atom and the S and SeS atoms make relatively small contributions to the major valence band near the Fermi level of the WSeS structure. The influence of the s orbitals of W, Se, and S on both the valence and conduction bands is negligible and occurs far from the Fermi level. Note that there are many locations outside the Fermi energy level where the d orbitals of the W atoms overlap with the p orbitals of Se and S. These orbitals are not in the vicinity of the Fermi energy level and do not contribute to the transport of charge carriers.

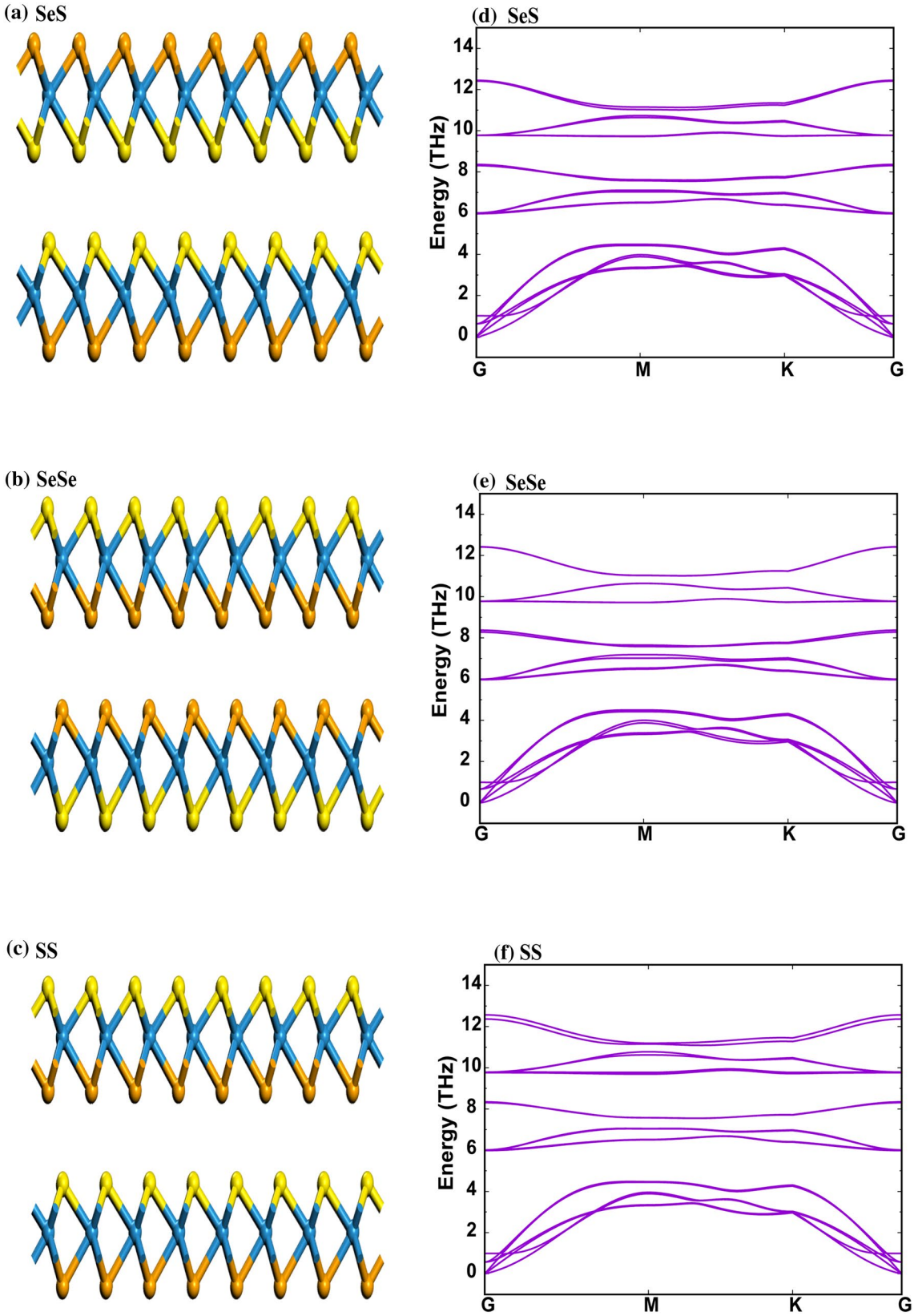

Fig. 1 Janus WeSeS bilayer structures with (a) SeS, (b) SeSe, and (c) SS stacking modes. The blue, brown, and yellow balls represent W, Se, and S atoms, respectively. Phonon spectra of the (d) SeS, (e) SeSe, and (f) SS stacking structures (Color figure online).

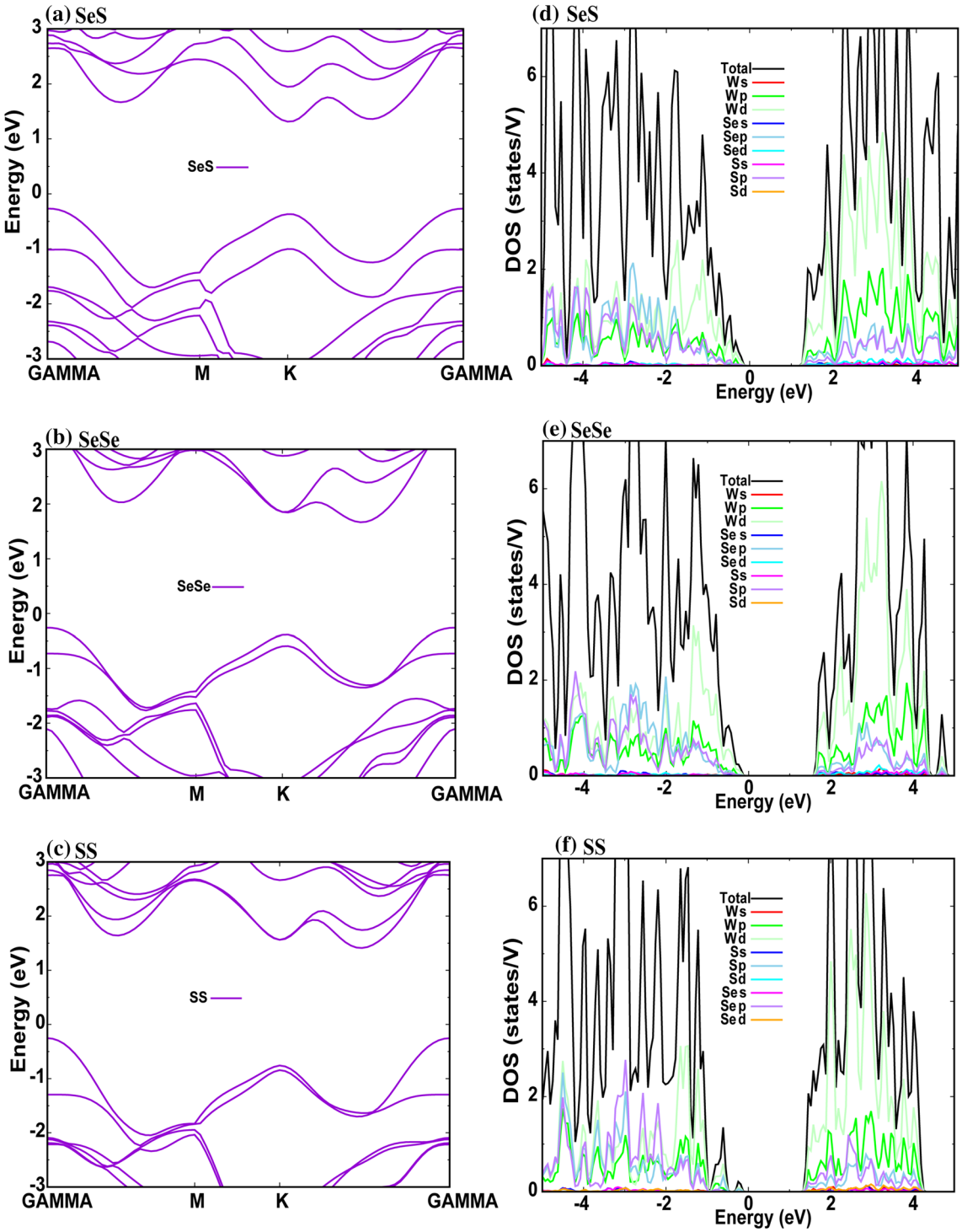

Fig. 2 Band structures of the (a) SeS, (b) SeSe, and (c) SS stacking structures calculated by HSE06. Projected DOS values for the (d) SeS, (e) SeSe, and (f) SS stacking structures.

Seebeck Coefficients

Figure 3a, b, and c show the variation in the n-type doping Seebeck coefficient with the concentration at different temperatures for the WSeS-based structures with SeS, SeSe, and SS stacking. Figure 3d, e, and f show the variation in the p-type doping Seebeck coefficient with the concentration at different temperatures for the WSeS structures with SeS, SeSe, and SS stacking. The calculated outcomes lead us to conclude that the Seebeck coefficient decreases with

Table I Calculated effective mass, elastic modulus, deformation potential constant, and relaxation time of electrons and holes for the Janus WSeS bilayer

	me m0	mh m0	C2DJm-2	Ee eV	Eh eV	τ_e fs	τ_h fs	μ_e cm^{2}V^{-1} s^{-1}	μ_h cm^{2}V^{-1} s^{-1}
SeS	0.532	0.966	274.08	7.33	2.696	77.41	315.15	269.96	605.26
SeSe	0.509	0.899	280.32	9.346	3.986	50.90	152.20	185.54	293.46
SS	0.586	0.729	280.64	8.606	1.720	52.20	195.62	165.28	497.83
Monolayer[31]	0.33	0.45	136.49	10.890	4.91	80	20	120.49	318.75

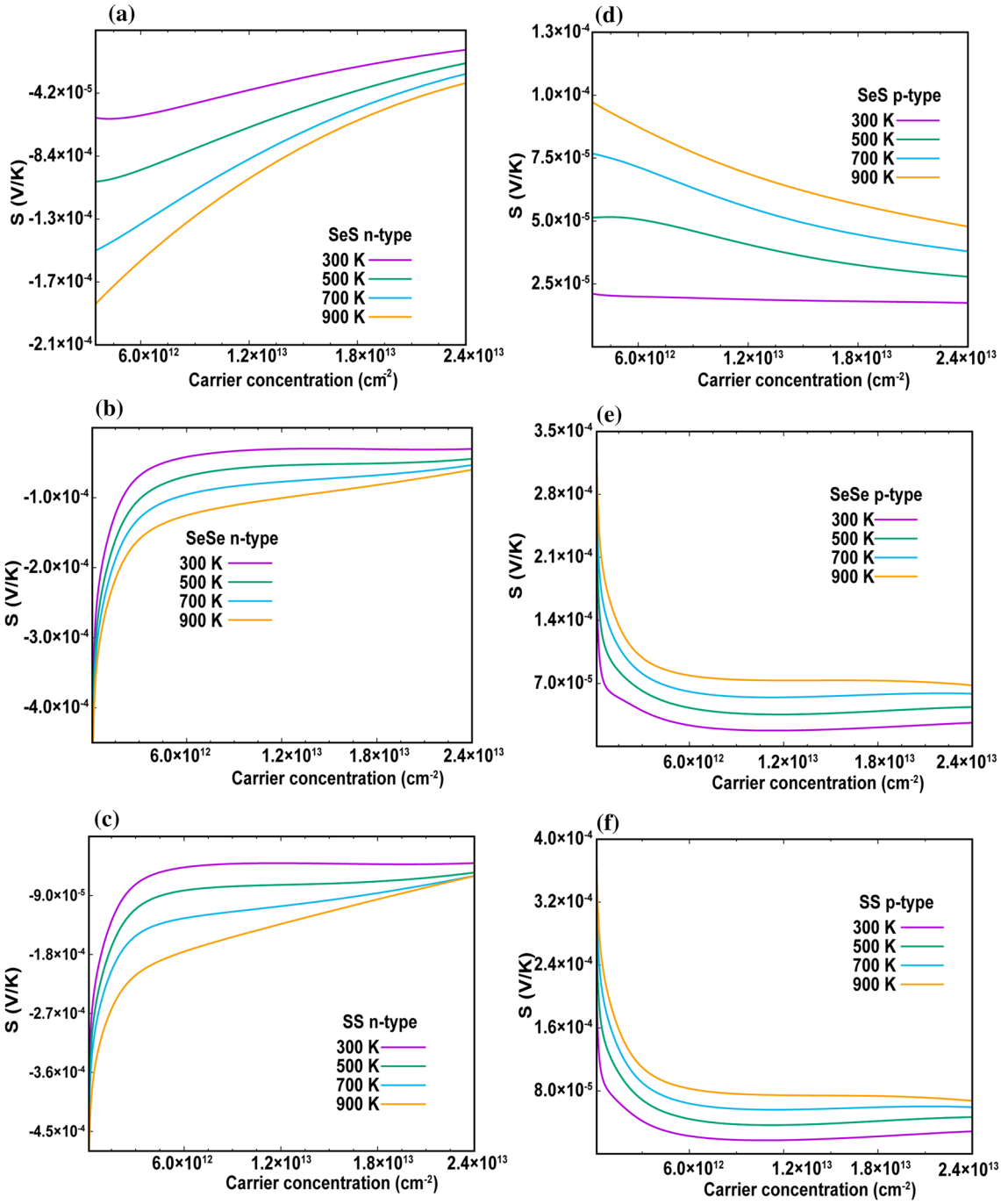

Fig. 3 Seebeck coefficients for the (a) SeS, (b) SeSe, and (c) SS stacking structures with n-type doping at different temperatures. Seebeck coefficients for the (d) SeS, (e) SeSe, and (f) SS stacking structures with p-type doping at different temperatures.

increasing carrier concentration. The Seebeck coefficient can be related to the carrier concentration as follows: $S = k_B\left[\ln\left({}^{N}/_{n}\right) + 2.5 - r\right]\Big/e$, where N, n, r, and e are the effective DOS near the Fermi level, carrier concentration, scattering mechanism parameter, and electron charge, respectively.[33] The aforementioned equation shows that the Seebeck coefficient decreases with increasing concentration.[34] In addition, the impact of the temperature on the Seebeck coefficient cannot be neglected. Within the free-electron theory approximation, the Seebeck coefficient S is directly related to the temperature T as follows: $S = \left(8\pi^2 k_B^2/3eh^2\right)m * T(\pi/3n)^{2/3}$. Note that this equation shows that the Seebeck coefficient is proportional to the temperature, and Fig. 3 shows that the Seebeck coefficients increase with the temperature.

Electrical Conductivity

σ/τ can be obtained using Boltztrap2, and the relaxation time $\tau = 2\hbar^3 C\big/\left(3k_B T m^* E_l^2\right)$ can be determined from Eq. 3. These two results can be used to determine the electrical conductivity. Figure 4 shows the relationship between the

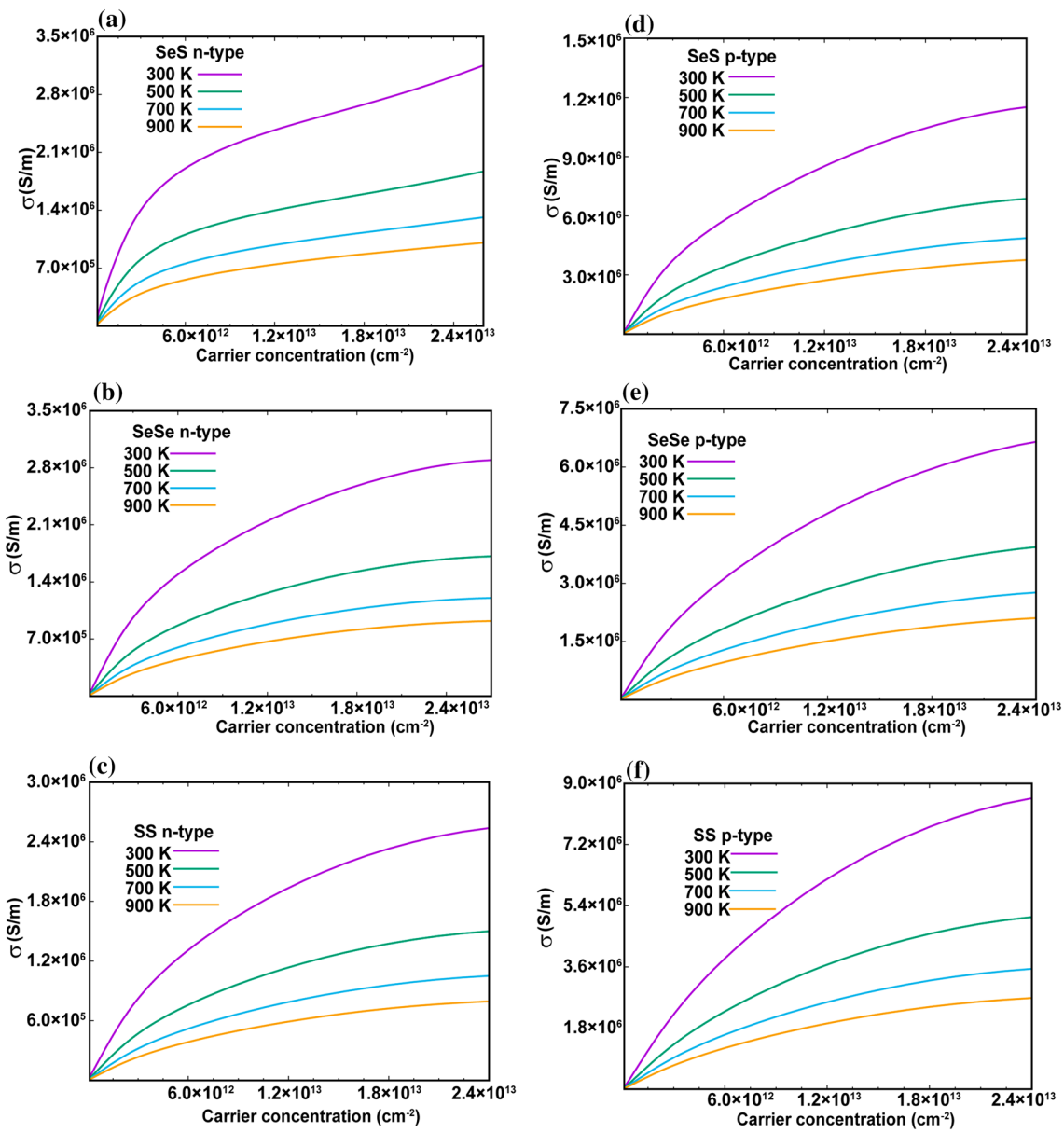

Fig. 4 Conductivity of the (a) SeS, (b) SeSe, and (c) SS stacked structures with n-type doping at different temperatures. Conductivity of the (d) SeS, (e) SeSe, and (f) SS stacked structures with p-type doping at different temperatures.

electrical conductivity and the doping concentration. Figure 4a, b, and c show the electrical conductivity of the SeS, SeSe, and SS structures versus the n-type doping concentrations, respectively. Figure 4a, b, and c show that at a constant temperature, the electrical conductivity increases with the carrier concentration. Figure 4d, e and f show the electrical conductivity of the Se, SeSe, and SS structures as a function of the p-doping concentration. The extracted results lead us to conclude that the carrier conduction paths between the atoms increase with the carrier concentration, which effectively changes the carrier transport properties.[32] Thus, it is reasonable that a high doping concentration produces a strong conductive pattern.

Figure 4 shows that holding all other conditions fixed, the SeS structure with p-type doping has the highest electrical conductivity and the SS structure with n-type doping has the lowest electrical conductivity. This effect is attributed to the difference in the relaxation times of these structures: the electrical conductivity can be related to the relaxation time

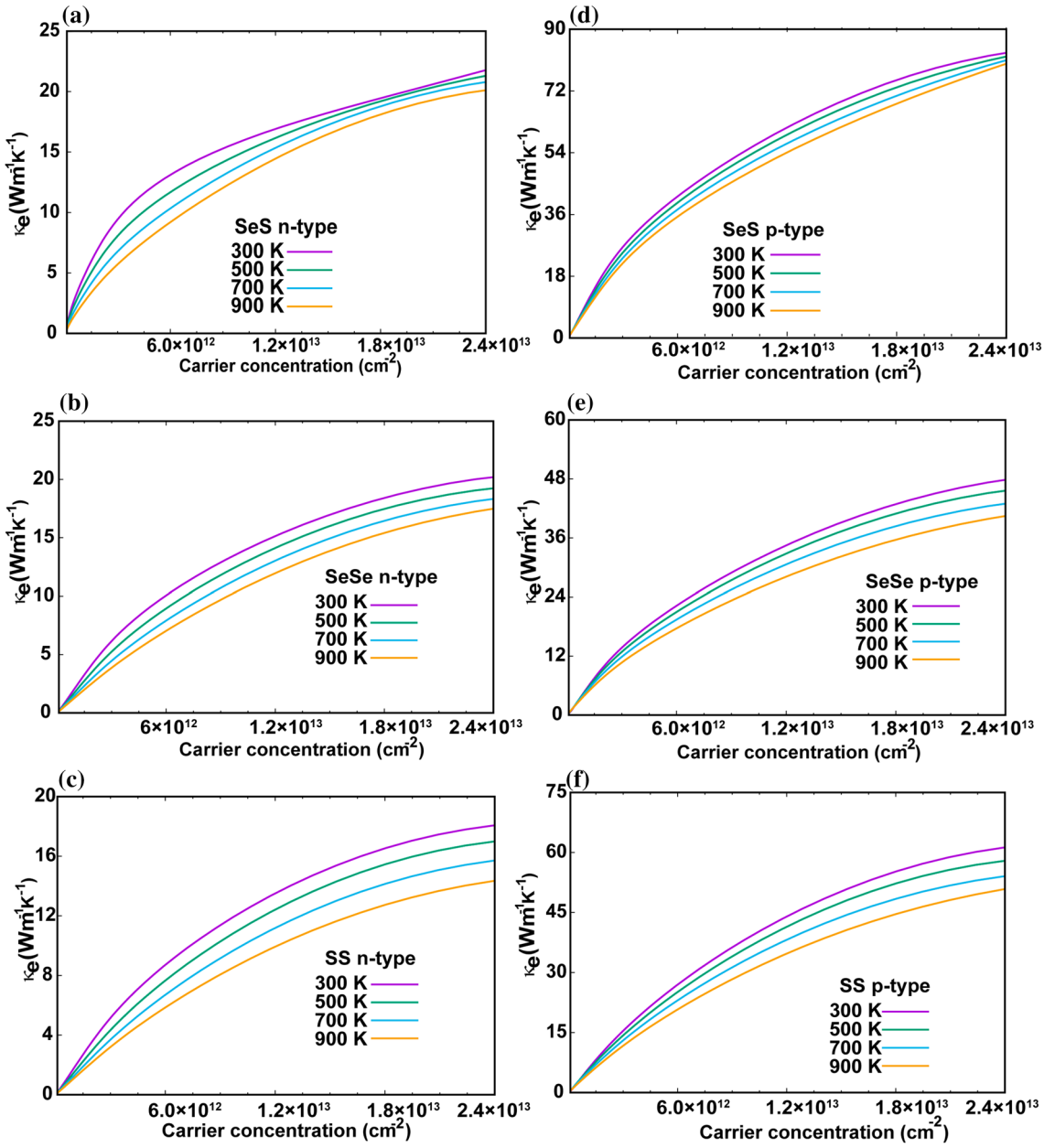

Fig. 5 Electronic thermal conductivity of the (a) SeS, (b) SeSe, and (c) SS stacked structures with n-type doping at different temperatures. Electronic thermal conductivity of the (d) SeS, (e) SeSe, and (f) SS stacked structures with p-type doping for electronic thermal conductivity at different temperatures.

as $\sigma = e^2 \int \tau\left(\vec{k}\right) v\left(\vec{k}\right) v\left(\vec{k}\right) \left[-\partial f^0\left(\varepsilon_k\right)/\varepsilon_k\right] \mathrm{d}\varepsilon \Big/ \Omega$, where Ω represents the volume of the unit cell, $\tau\left(\vec{k}\right)$ represents the relaxation time, $v\left(\vec{k}\right)$ represents the group velocity, ε_f represents the Fermi energy, and f^0 is the Fermi–Dirac distribution function.[35] The results presented in Table I show that the SeS structure with p-type doping has the greatest relaxation time and therefore the highest electrical conductivity, and vice versa. Thus, the electrical conductivity is positively correlated with the carrier relaxation time: the larger the carrier relaxation time, the higher the electrical conductivity.

Thermal Conductivity

Electronic Thermal Conductivity

The influence of the carrier concentration on the thermal conductivity of the material is also analyzed. Notably, the total thermal conductivity has two components: the electronic thermal conductivity (κ_e) and the lattice thermal conductivity (κ_l). The change in the electronic thermal conductivity distribution with the carrier concentration is calculated at different temperatures. These results are presented graphically in Fig. 5, showing trends with the doping concentration. Figure 5a, b, and c show the electronic thermal conductivity of the n-doped material as a function of the carrier concentration at different temperatures. Figure 5d, e, and f show the total thermal conductivity and the electronic thermal conductivity of the p-doped material as a function of the carrier concentration at different temperatures. The extracted outcomes show that the electrical thermal conductivity of the Janus-based WSeS gradually increases with the doping concentration. The Boltzmann transport equation can be used to calculate the electronic thermal conductivity as $\kappa_e = \pi^2 n k_B^2 T \tau_e / 3m_0$.[36] Hence, it can be concluded that a high doping concentration leads to high electronic thermal conductivity. The electronic thermal conductivity decreases with increasing temperature. The electronic thermal conductivity and electrical conductivity are related by the Wiedemann–Franz law[37,38] $\kappa_e = L\sigma T$, where L is the Lorentz constant. The electronic thermal conductivity depends on the temperature and electrical conductivity. Figure 5 shows that the electronic conductivity decreases with increasing temperature. In summary, the electronic thermal conductivity of electrons decreases with increasing temperature.

Lattice Thermal Conductivity

The phonon kinetic theory can be used to express the lattice thermal conductivity as $\kappa_l = C_\lambda \upsilon_\lambda^2 \tau_\lambda / 3$, where υ_λ is the phonon velocity, τ_λ is the phonon relaxation time, $C_\lambda = \sum_\lambda 9R\left(T/\Theta_D\right)^3 \int_0^{\Theta_D} y^4 e^y / (e^y - 1)^2 dy$ is the heat capacity distribution, R is the ideal gas constant, λ is the phonon mode, Θ_D is the Debye temperature, and $y = \Theta_D / T$.[39]

The group velocity of phonons is one of the determining factors for the thermal conductivity of phonons. Figure 6a, b, and c show the trend in the phonon group velocity with the frequency for the three structures of Janus-based WSeS bilayers. The phonon group velocity along the x- and y-direction is approximately 150 THz*Angstrom for the SeS structure and has a higher value of approximately 300 THz*Angstrom for the SeSe and SS structures.

The phonon relaxation time also influences the thermal conductivity of phonons. Thus, the phonon relaxation times of the three structures vary across the frequency range, as shown in Fig. 7a, b, and c. The phonon relaxation time of the SeS structure is considerably larger than that of the SeSe and SS structures. The relaxation time of the SeSe structure is lower than that of the SS structure. Figure 7 shows that the SeS structure has a relatively large relaxation time in the high-frequency range. The phonon relaxation time can be expressed as follows:$1/\tau = 1/\tau_{PP} + 1/\tau_{PB} + 1/\tau_{PD}$, where $1/\tau_{pp}$,$1/\tau_{PB}$, and $1/\tau_{PD}$ are the contributions from phonon–phonon scattering, phonon-boundary scattering, and phonon-defect scattering, respectively.[40,41]

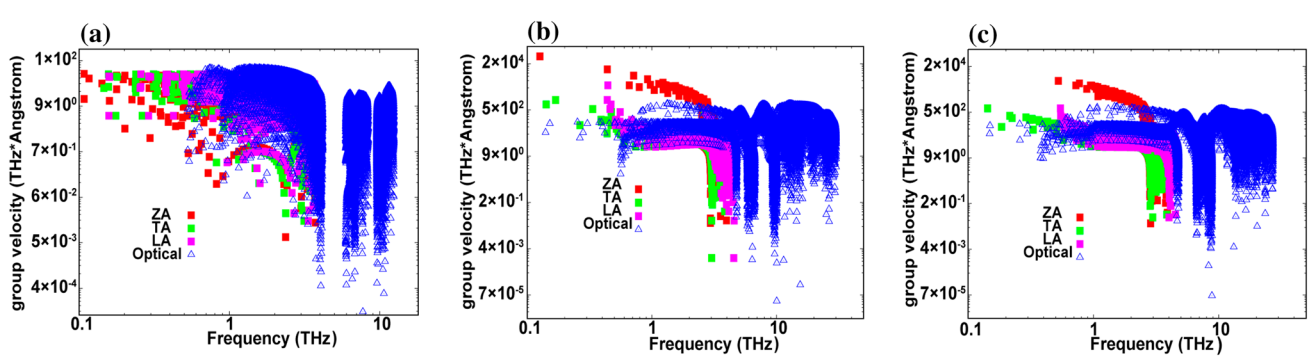

Fig. 6 Frequency-dependent velocities of phonon groups for the (a) SeS, (b) SeSe, and (c) SS stacking modes.

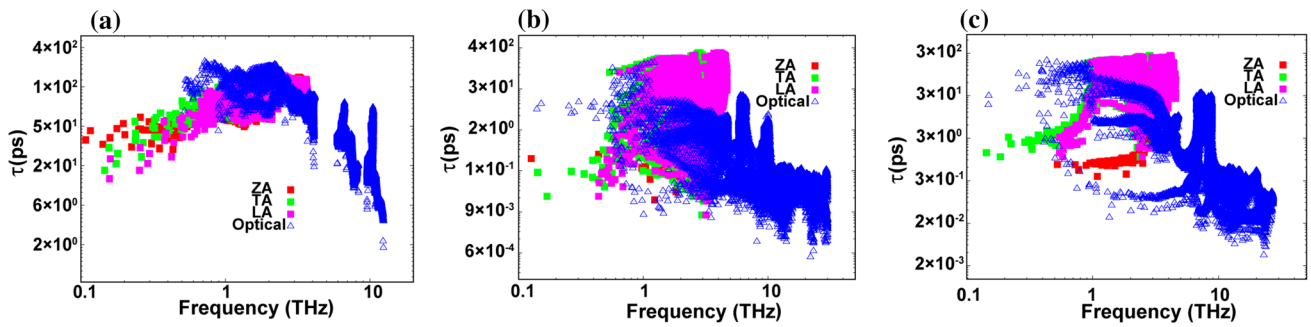

Fig. 7 Frequency dependence of the phonon relaxation time for the (a) SeS, (b) SeSe, and (c) SS stacking modes.

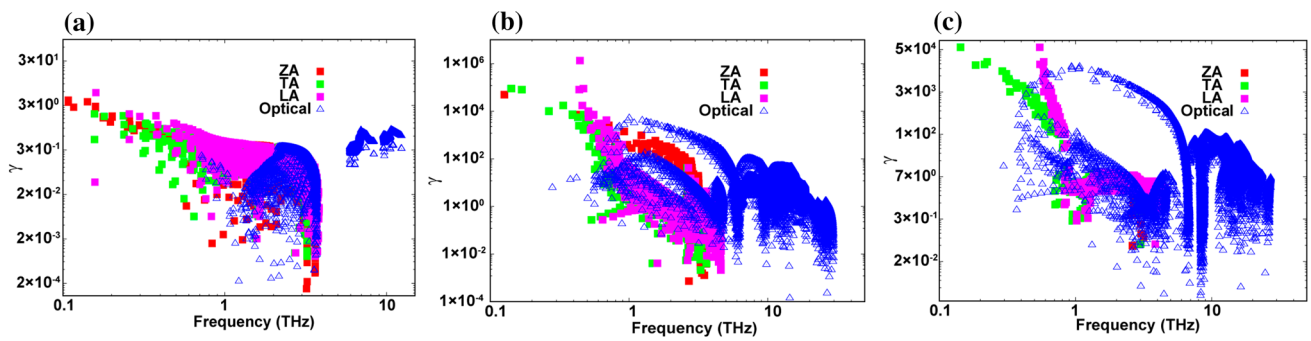

Fig. 8 (a) Variation in the Grünigsen constant with frequency for the (a) SeS, (b) SeSe, and (c) SS stacking structures.

The Grüneisen constant can be used to evaluate the anharmonicity of materials and as a general measure of the scattering rate. Consequently, the higher the Grüneisen constant, the lower the thermal conductivity of the phonons.[42] Figure 8a, b, and c show the frequency-dependent Grüneisen constants of the SeS, SeSe, and SS structures. The SeSe structure has the highest Grüneisen constant over the entire frequency range, followed by the SS structure and then the SeS structure. Therefore, the phonon relaxation time is the largest for the SeSe structure, followed by the SS structure and then the SeS structure.

Figure 9 shows the lattice thermal conductivity κ_l of the SeS, SeSe, and SS structures, where κ_l decreases with increasing temperature. Note that the SeSe structure has the highest phonon group velocity and the shortest phonon relaxation time; by comparison, the SeS structure possesses the lowest phonon group velocity and the longest phonon relaxation time, which leads to the largest κ_l. Similarly, at a fixed temperature, the configuration of SeSe results in the lowest κ_l, as shown in Fig. 9. This effect is ascribed to the significant enhancement of phonon–phonon interactions at elevated temperatures. Thus, the higher the temperature, the stronger the phonon–phonon interaction, whereas phonons are prevented from participating in heat transfer from high-temperature to low-temperature regions.[42] Therefore, the lattice thermal conductivity decreases as the temperature increases.

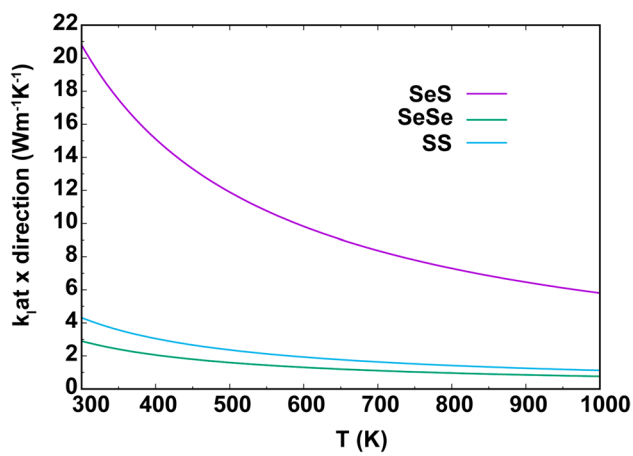

Fig. 9 The lattice thermal conductivity versus the temperature for the SeS, SeSe, and SS stacking structures.

Figures of Merit

As all the transport properties have been determined, the figure of merit, *ZT*, of the WSeS can be calculated. Figure 10

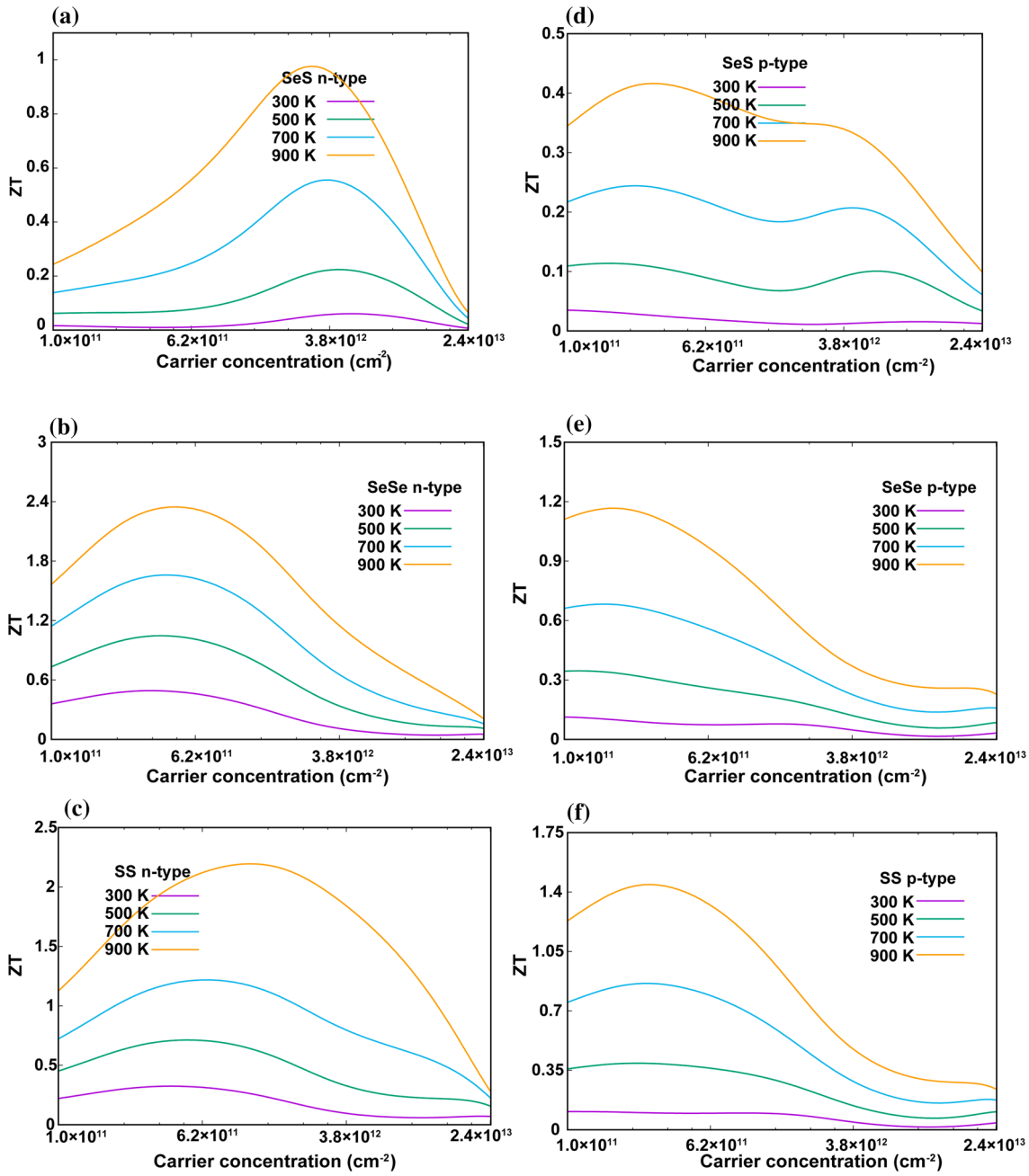

Fig. 10 *ZT* of the (a) SeS, (b) SeSe, and (c) SS stacked structures with n-type doping at different temperatures. *ZT* of the (d) SeS, (e) SeSe, and (f) SS stacked structures with p-type doping at different temperatures.

shows the variation in *ZT* for the n- and p-type doped materials in the *x*- and *y*-direction as a function of the carrier concentration at different temperatures. As the carrier concentration increases, *ZT* first rises to a peak and then decreases. *ZT* increases with the temperature. *ZT* is higher for n-type doping than p-type doping, holding all other conditions constant. The highest *ZT* peak for n-type doping is obtained for the SeSe structure, which possesses the lowest thermal conductivity and highest electrical conductivity. In conclusion, the SeSe structure exhibits a *ZT* of 2.4 with an n-type doping concentration of 5×10^{11} cm^{-3} at a temperature of 900 K. Patel et al. determined the thermoelectric properties of monolayer WSeS using first-principles calculations based on the semiclassical Boltzmann transport theory.[16] A *ZT* of approximately 0.25 was determined at 900 K due to the extraordinary Seebeck coefficient and high electrical conductivity of the material. Kumar et al. used the same methods to calculate a *ZT* of 0.8 for monolayer WSe_2 at 1200 K, which results

from the low thermal conductivity of the material.[43] Huang et al. determined the *ZT* of WSe_2 at 500 K using ab initio calculations and ballistic transport theory.[44] These results can be explained in terms of the presence of additional valleys in the electron energy band structure near the k-point at high temperatures. The results of our study show that the Janus WSeS bilayer has superior thermoelectric properties to those of WSe_2 or WSeS monolayers.

Conclusion

In summary, first-principles calculations and the Boltzmann semiclassical transport theory were employed to systematically investigate the geometry, band structure distribution, electrical conductivity, thermal conductivity, Seebeck coefficient, and figures of merit of Janus-based WSeS bilayers with SeS, SeSe, and SS stacking. The small deformation potential constant and large elastic modulus of a monolayer results in an enhanced carrier relaxation time; thus, Janus-based WSeS bilayer structures possess excellent electrical transport capability and thermoelectric properties. Moreover, n-type doping of the SeSe structure results in excellent thermoelectric performance, with a *ZT* of 2.4 due to high electrical conductivity and low thermal conductivity at 900 K at an n-doping concentration of $5 \times 10^{11} cm^{-3}$. These calculated outcomes can be used for other two-dimensional materials and can provide useful theoretical guidance for optimizing various thermoelectric properties.

Supplementary Information The online version contains supplementary material available at https://doi.org/10.1007/s11664-022-09851-w.

Author contribution All the authors contributed to the writing of this manuscript.

Data Availability All the data presented in this study are available upon request by contacting the corresponding author.

Conflict of interest The authors declare that they have no known competing financial interests or personal relationships that could appeared to influence the work reported in this paper.

References

1. W.Y. Chen, X.L. Shi, J. Zou, and Z.G. Chen, Thermoelectric Coolers: Progress, Challenges, and Opportunities. *Small Methods* 6, 2101235 (2022).
2. F. Tohidi, S. Ghazanfari Holagh, and A. Chitsaz, Thermoelectric Generators: A Comprehensive Review of Characteristics and Applications. *Appl. Therm. Eng.* 201, 117793 (2022).
3. Z. Bu, X. Zhang, Y. Hu, Z. Chen, S. Lin, W. Li, C. Xiao, and Y. Pei, A Record Thermoelectric Efficiency in Tellurium-Free Modules for Low-Grade Waste Heat Recovery. *Nat. Commun.* 13, 237 (2022).
4. K. Li, X. Sun, Y. Wang, J. Wang, X. Dai, G. Li, and H. Wang, All-in-one Single-Piece Flexible Solar Thermoelectric Generator with Scissored Heat Rectifying p-n Modules. *Nano Energy* 93, 106789 (2022).
5. Y. Zhu, D.W. Newbrook, P. Dai, C.H.K. de Groot, and R. Huang, Artificial Neural Network Enabled Accurate Geometrical Design and Optimisation of Thermoelectric Generator. *Appl. Energy* 305, 117800 (2022).
6. S. Wen, J. Ma, A. Kundu, and W. Li, Large Lattice Thermal Conductivity, Interplay Between Phonon-Phonon, Phonon-Electron, and Phonon-Isotope Scatterings, and Electrical Transport in Molybdenum From First Principles. *Phys. Rev. B* 102, 064303 (2020).
7. G. Deokar, D. Vignaud, R. Arenal, P. Louette, and J.F. Colomer, Synthesis and Characterization of MoS_2 Nanosheets. *Nanotechnology* 27, 075604 (2016).
8. Q. Tang and Z. Zhou, Graphene-Analogous Low-Dimensional Materials. *Prog. Mater Sci.* 58, 1244 (2013).
9. A.I. Siahlo, N.A. Poklonski, A.V. Lebedev, I.V. Lebedeva, A.M. Popov, S.A. Vyrko, A.A. Knizhnik, and Y.E. Lozovik, Structure and Energetics of Carbon, Hexagonal Boron Nitride, and Carbon/Hexagonal Boron Nitride Single-Layer and Bilayer Nanoscrolls. *Phys. Rev. Mater.* 2, 036001 (2018).
10. N.A. Poklonski, S.A. Vyrko, A.I. Siahlo, O.N. Poklonskaya, S.V. Ratkevich, N.N. Hieu, and A.A. Kocherzhenko, Synergy of Physical Properties of Low-Dimensional Carbon-Based Systems for Nanoscale Device Design. *Mater. Res. Express* 6, 042002 (2019).
11. T. Georgiou, L. Britnell, P. Blake, R.V. Gorbachev, A. Gholinia, A.K. Geim, C. Casiraghi, and K.S. Novoselov, Graphene Bubbles with Controllable Curvature. *Appl. Phys. Lett.* 99, 093103 (2011).
12. Z.H. Ni, T. Yu, Y.H. Lu, Y.Y. Wang, Y.P. Feng, and Z.X. Shen, Uniaxial Strain on Graphene: Raman Spectroscopy Study and Band-Gap Opening. *ACS Nano* 2, 2301 (2008).
13. Z. Wu, K. Yin, J. Wu, Z. Zhu, J.A. Duan, and J. He, Recent Advances in Femtosecond Laser-Structured Janus Membranes with Asymmetric Surface Wettability. *Nanoscale* 13, 2209 (2021).
14. X. Zheng, S. Kang, K. Wang, Y. Yang, D.-G. Yu, F. Wan, G.R. Williams, and S.W.A. Bligh, Combination of Structure-Performance and Shape-Performance Relationships for Better Biphasic Release in Electrospun Janus Fibers. *Int. J. Pharm.* 596, 120203 (2021).
15. G. Chaney, A. Ibrahim, F. Ersan, D. Çakır, and C. Ataca, Comprehensive Study of Lithium Adsorption and Diffusion on Janus Mo/WXY (X, Y = S, Se, Te) Using First-Principles and Machine Learning Approaches. *ACS Appl. Mater. Interfaces* 13, 36388 (2021).
16. A. Patel, D. Singh, Y. Sonvane, P.B. Thakor, and R. Ahuja, High Thermoelectric Performance in Two-Dimensional Janus Monolayer Material WS-X (X = Se and Te). *ACS Appl. Mater. Interfaces* 12, 46212 (2020).
17. R. Chaurasiya, S. Tyagi, N. Singh, S. Auluck, and A. Dixit, Enhancing Thermoelectric Properties of Janus WSSe Monolayer by Inducing Strain Mediated Valley Degeneracy. *J. Alloys Compd.* 855, 157304 (2021).
18. D.M. Hoat, M. Naseri, N.N. Hieu, R. Ponce Pérez, J.F. Rivas Silva, T.V. Vu, and G.H. Cocoletzi, A Comprehensive Investigation on Electronic Structure, Optical and Thermoelectric Properties of the HfSSe JANUS Monolayer. *J. Phys. Chem. Solids* 144, 109490 (2020).
19. G. Kresse and J. Furthmüller, Efficient Iterative Schemes for Ab Initio Total-Energy Calculations using a Plane-Wave Basis Set. *Phys. Rev. B* 54, 11169 (1996).
20. S. Duhm, G. Heimel, I. Salzmann, H. Glowatzki, R.L. Johnson, A. Vollmer, J.P. Rabe, and N. Koch, Orientation-Dependent

Ionization Energies and Interface Dipoles in Ordered Molecular Assemblies. *Nat. Mater.* 7, 326 (2008).
21. P. Deák, B. Aradi, T. Frauenheim, E. Janzén, and A. Gali, Accurate Defect Levels Obtained from the HSE06 Range-Separated Hybrid Functional. *Phys. Rev. B* 81, 153203 (2010).
22. G.K.H. Madsen, J. Carrete, and M.J. Verstraete, BoltzTraP2, a Program for Interpolating Band Structures and Calculating Semi-Classical Transport Coefficients. *Comput. Phys. Commun.* 231, 140 (2018).
23. G.K.H. Madsen, D.J. Singh, and BoltzTraP, A Code for Calculating Band-Structure Dependent Quantities. *Comput. Phys. Commun.* 175, 67 (2006).
24. J. Bardeen and W. Shockley, Deformation Potentials and Mobilities in Non-Polar Crystals. *Phys. Rev.* 80, 72 (1950).
25. J. Moellmann and S. Grimme, DFT-D3 Study of Some Molecular Crystals. *J. Phys. Chem. C* 118, 7615 (2014).
26. A. Togo and I. Tanaka, First Principles Phonon Calculations in Materials Science. *Scripta Mater.* 108, 1 (2015).
27. A. Togo, L. Chaput, and I. Tanaka, Distributions of Phonon Lifetimes in Brillouin Zones. *Phys. Rev. B* 91, 094306 (2015).
28. J. Hafner, Ab-Initio Simulations of Materials using VASP: Density-Functional Theory and Beyond. *J. Comput. Chem.* 29, 2044 (2008).
29. D. Malko, C. Neiss, F. Viñes, and A. Görling, Competition for Graphene: Graphynes with Direction-Dependent Dirac Cones. *Phys. Rev. Lett.* 108, 086804 (2012).
30. W. Jing, A. Rahman, A. Ghosh, G. Klimeck, and M. Lundstrom, On the Validity of the Parabolic Effective-Mass Approximation for the I-V Calculation of Silicon Nanowire Transistors. *IEEE Trans. Electron Devices* 52, 1589–1595 (2005).
31. B. Hou, Y. Zhang, H. Zhang, H. Shao, C. Ma, X. Zhang, Y. Chen, K. Xu, G. Ni, and H. Zhu, Room Temperature Bound Excitons and Strain-Tunable Carrier Mobilities in Janus Monolayer Transition-Metal Dichalcogenides. *J. Phys. Chem. L* 11, 3116 (2020).
32. B. Song, L. Liu, and C. Yam, Suppressed carrier recombination in Janus MoSSe bilayer stacks: A time-domain Ab initio study. *J. Phys. Chem. L* 10, 5564 (2019).
33. N. Wang, M. Li, H. Xiao, Z. Gao, Z. Liu, X. Zu, S. Li, and L. Qiao, Band Degeneracy Enhanced Thermoelectric Performance in Layered Oxyselenides by First-Principles Calculations. *npj Comput. Mater.* 7, 18 (2021).
34. N. Wang, M. Li, H. Xiao, H. Gong, Z. Liu, X. Zu, and L. Qiao, Optimizing the Thermoelectric Transport Properties of Bi_2O_2Se Monolayer Via Biaxial Strain. *Phys. Chem. Chem. Phys.* 21, 15097 (2019).
35. F.Q. Wang, Y. Guo, Q. Wang, Y. Kawazoe, and P. Jena, Exceptional Thermoelectric Properties of Layered $GeAS_2$. *Chem. Mater.* 29, 9300 (2017).
36. S.Y. Yue, X. Zhang, S. Stackhouse, G. Qin, E. Di Napoli, and M. Hu, Methodology for Determining the Electronic Thermal Conductivity of Metals Via Direct Nonequilibrium Ab Initio Molecular Dynamics. *Phys. Rev. B* 94, 075149 (2016).
37. W.L. Tao, J.Q. Lan, C.E. Hu, Y. Cheng, J. Zhu, and H.Y. Geng, Thermoelectric Properties of Janus MXY (M = Pd, Pt; X, Y = S, Se, Te) Transition-Metal Dichalcogenide Monolayers From First Principles. *J. Appl. Phys.* 127, 035101 (2020).
38. N. Stojanovic, D.H.S. Maithripala, J.M. Berg, and M. Holtz, Thermal Conductivity in Metallic Nanostructures at High Temperature: Electrons, Phonons, and the Wiedemann-Franz law. *Phys. Rev. B* 82, 075418 (2010).
39. L. Zhang and G. Ouyang, Size-Dependent Thermal Boundary Resistance and Thermal Conductivity in Si/Ge core–Shell Nanowires. *IEEE Trans. Electron Devices* 65, 361 (2017).
40. D.L. Nika, E.P. Pokatilov, A.S. Askerov, and A.A. Balandin, Phonon Thermal Conduction in Graphene: Role of Umklapp and Edge Roughness Scattering. *Phys. Rev. B* 79, 155413 (2009).
41. D.O. Lindroth and P. Erhart, Thermal Transport in Van Der Waals Solids from First-Principles Calculations. *Phys. Rev. B* 94, 115205 (2016).
42. F.Q. Wang, M. Hu, and Q. Wang, Ultrahigh Thermal Conductivity of Carbon Allotropes with Correlations with the Scaled Pugh Ratio. *J. Mater. Chem. A* 7, 6259 (2019).
43. S. Kumar and U. Schwingenschlögl, Thermoelectric Response of Bulk and Bonolayer $MoSe_2$ and WSe_2. *Chem. Mater.* 27, 1278 (2015).
44. W. Huang, H. Da, and G. Liang, Thermoelectric Performance of MX_2 (M = Mo, W; X = S, Se) Monolayers. *J. Appl. Phys.* 113, 104304 (2013).

Publisher's Note Springer Nature remains neutral with regard to jurisdictional claims in published maps and institutional affiliations.